

## Research Article

# Optimizing the Crystallinity of Heptazine-Based Crystalline Carbon Nitride by Regulating Temperature for Enhanced Photocatalytic H<sub>2</sub> Evolution

Haomiao Tang,<sup>1</sup> Wenbin Wang,<sup>1</sup> Jun Zhou,<sup>1,2</sup> Tiantian Li,<sup>3</sup> and Zhu Shu <sup>1,2</sup>

<sup>1</sup>Engineering Research Center of Nano-Geomaterials of Ministry of Education, Faculty of Materials Science and Chemistry, China University of Geosciences, 388 Lumo Road, Wuhan 430074, China

<sup>2</sup>Hubei Three Gorges Laboratory, 1 Mazongling Road, Yichang 443007, China

<sup>3</sup>College of Chemistry and Chemical Engineering, Henan Province Key Laboratory of Utilization of Non-Metallic Mineral in the South of Henan, Xinyang Normal University, Xinyang 464000, China

Correspondence should be addressed to Zhu Shu; shuzhu@cug.edu.cn

Received 4 July 2022; Revised 25 August 2022; Accepted 26 September 2022; Published 18 November 2022

Academic Editor: Fengqiang Sun

Copyright © 2022 Haomiao Tang et al. This is an open access article distributed under the Creative Commons Attribution License, which permits unrestricted use, distribution, and reproduction in any medium, provided the original work is properly cited.

Polymeric carbon nitride (PCN), as a metal-free photocatalyst, has drawn wide attention in the photocatalytic H<sub>2</sub> evolution. However, the photocatalytic activity of directly synthesized PCN is limited by its low crystallinity. Currently, regulating the melon-based PCN into tri-s-triazine-based crystalline PCN to further optimize its structure has been proved to effectively improve its photocatalytic activity. The heptazine-based crystalline carbon nitride, potassium poly(heptazine imide) (abbreviated as K-PHI), has been used in photocatalytic H<sub>2</sub> evolution benefiting from its high crystallinity, as the high crystallinity narrows the bandgap and increases the light capture efficiency and increases the charge mobility. Nevertheless, the effect of synthesis temperature on crystallinity has not yet been reported. In this work, the effect of temperature on the crystallinity of heptazine-based crystalline carbon nitride was studied by one-step synthesis at different temperatures. It shows that the heptazine-based crystalline structure appears when the temperature exceeds 540°C. Additionally, the crystallinity of all samples is gradually improved with increasing temperature until the sample begins to decompose beyond 630°C. The sample synthesized at 630°C demonstrates the highest photocatalytic H<sub>2</sub> evolution rate of 1.798 mmol h<sup>-1</sup> g<sup>-1</sup> under visible light irradiation, which is 31.5 times that of bulk PCN. Based on systematic material characterizations, the mechanism of the effect of synthesis temperature on crystallinity and the contribution of crystallinity to photocatalytic efficiency were revealed.

## 1. Introduction

Polymeric carbon nitride (PCN), also named graphitic carbon nitride (g-C<sub>3</sub>N<sub>4</sub>), is a metal-free photocatalyst consisting mainly of carbon and nitrogen [1]. As a visible light photocatalyst, PCN is regarded as one of the most active phases [2, 3]. PCN can be easily prepared by precursors containing carbon and nitrogen such as cyanamide, dicyandiamide, melamine, and urea [4–8]. Additionally, compared with photocatalysts based on metallic elements, the synthesis of PCN is cheaper and it can be produced on a larger scale [8–10]. These special properties allow it to exhibit potential applications in a variety of fields, such as photocatalytic water splitting for

hydrogen [11, 12], degradation of organic pollutants [13, 14], photocatalytic reduction of CO<sub>2</sub> [15, 16], photocatalytic antibacterial [17, 18], and biomedical sciences [19]. The PCN was first used in photocatalytic hydrogen production under visible light irradiation in 2009 [6]. Since then, the PCN has drawn wide attention in photocatalytic H<sub>2</sub> evolution based on the unique graphite-like structure, medium band-gap structure (2.7 eV), excellent chemical stability, and thermal stability [20, 21]. However, melon-based PCN synthesized by thermal condensation of nitride precursors was limited by its low crystallinity, which leads to a narrow visible light absorption range, severe electron-hole pair compounding, and fewer active sites. Therefore, it is

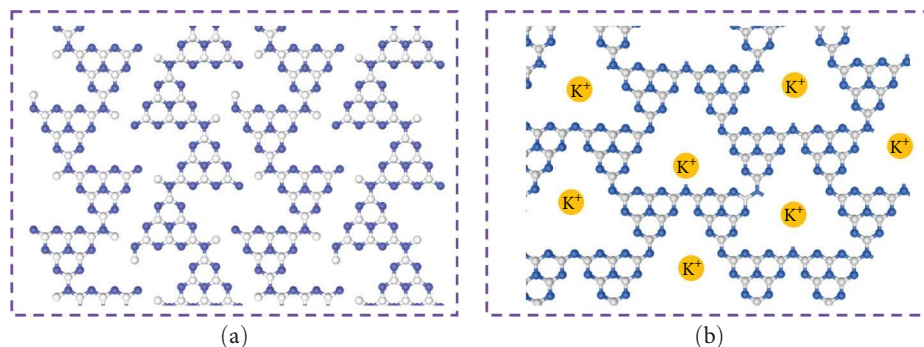


FIGURE 1: (a) The structure of melon-based PCN. (b) The structure of heptazine-based K-PHI.

necessary to enhance its crystallinity and connection patterns [12, 22].

Potassium poly(heptazine imide) (abbreviated as K-PHI) is a 2D-layered crystalline CN, which has a higher crystallinity and more complete in-plane structure compared with melon-based CN (Figure 1) [23, 24]. Unlike PCN directly synthesized by thermal condensation, the K-PHI is typically synthesized by a molten-salt (MS) approach that employs alkali metal halides as a high-temperature solvent and structure-directing agent, which caused the formation of highly crystalline structure and nanostructured morphology. Compared with melon-based PCN, the K-PHI exhibits significantly improved photocatalytic  $H_2$  evolution activity benefiting from its enhanced separation and transfer efficiency of photoinduced charges owned to more complete in-plane structure and higher crystallinity. A variety of approaches for the synthesis of highly crystalline K-PHI using alkali metal salts as MSs have been reported in previous studies. For instance, Ou et al. prepared crystalline PCN nanosheets by synthesizing PCN in LiCl–KCl molten salt and then exfoliating it via sonication for 15 hr in isopropanol [25]. Zeng et al. synthesized highly crystalline PCN by using KCl and LiCl as the MS system and melamine as the precursor [26]. In addition, highly crystalline  $g\text{-C}_3\text{N}_4$  hollow spheres were prepared by the MS method using KCl and LiCl as the MS system and cyanuric acid–melamine as a precursor [27].

Hence, it is a crucial task to start further research on K-PHI in the field of photocatalysis. On one hand, it is necessary to develop more efficient crystalline CN catalysts by modulating the specific surface area, reaction active sites, and charge conversion rate of crystalline CN. On the other hand, improving the degree of crystallinity of CN is also of great importance in improving the photocatalytic efficiency of CN [28]. At present, a large number of modulation studies have been carried out to improve the photocatalytic activity of K-PHI, including structural nanosizing [29], defect introduction [30], morphology adjusting [25], and interface design [31]. For example, Fan et al. obtained a highly efficient PCN–KCl nanosheet photocatalyst with the assistance of KCl [32]. He et al. prepared hollow sodium polyphosphate (SPP)-MS-CN nanotubes through a green one-step approach by SPP in situ modulated MS thermal condensation of melamine and directionally mediated triazine and heptazine units by the SPP content [33]. Li et al. synthesized the

crystalline isotype heptazine/triazine-based  $g\text{-C}_3\text{N}_4$  and investigated the interfacial interactions of its heterojunction by first principle calculations [31].

Crystallinity is responsible for the photocatalytic activity of CN, as high crystallinity is an important factor in reducing the number of carrier complex centers. In addition, as polymer photocatalysts, high crystallinity narrows the band-gap and increases the light capture efficiency, and increases the charge mobility due to the extended  $\pi$ -conjugated system and the off-domain  $\pi$  electrons [34–36]. Therefore, how to improve the crystallinity of the CN is, therefore, also a key issue. In addition to the above strategies, the synthesis conditions of materials may have an impact on the performance of K-PHI, including temperature, pressure, and atmosphere. As a consequence, it is important to get an in-depth knowledge of the properties under optimal synthesis conditions. The effect of synthesis conditions on the photocatalytic performance of CN has been studied in previous studies, but mainly for pristine CN, with less discussion of the crystallinity of crystalline CN. Calcination temperature is one of the more easily regulated synthesis conditions and has an intuitive effect on the synthesis of crystalline CN, whereas the interrelationship between temperature and crystallinity in the synthesis process and the influence law has been rarely reported.

Herein, the effect of synthesis temperature on the crystallinity of K-PHI was first studied. The K-PHI samples were synthesized using KCl as a structure-directing agent under different temperatures (540, 570, 600, and 630°C). The phase and chemical structures, optical and photoelectrical properties, and photocatalytic  $H_2$  evolution activities of the samples were systematically characterized. The influences of synthesis temperature on the crystallinity coupled with the resulting photocatalytic activity of K-PHI were investigated. It was found that the synthesis temperature aroused a significant effect on the crystallinity of K-PHI and that the degree of crystallinity increased with increasing temperature within a certain range. Furthermore, the relevant mechanism was also discussed. This study not only reveals the influence of the thermal synthesis temperature on the photocatalytic properties of crystalline CN, but also highlights the relationship between temperature and the influence of crystallinity on the microstructure of crystalline CN, i.e., crystallinity, which is an inspiration for the optimization of crystalline CN.

## 2. Experimental

**2.1. Materials.** All chemicals used in this study were of analytical grade. Melamine was purchased from Aladdin Co., Ltd. The KCl and alcohol were purchased from Sinopharm Chemical Reagent Co., Ltd. The chloroplatinic acid and triethanolamine were purchased from Vetec (Sigma-Aldrich).

**2.2. Preparation of Bulk PCN.** The bulk PCN was prepared in the conventional thermal condensation by directly heating melamine precursor in a muffle furnace. An amount of 10 g melamine was put into a ceramic crucible, which was wrapped with aluminum foil and calcined at 550°C for 2 hr with a heating rate of 10°C min<sup>-1</sup> in air atmosphere. Finally, the coarse yellow product was grounded into power and denoted as PCN.

**2.3. Preparation of K-PHI.** The K-PHI was prepared by a simple mixed calcination approach. About 2 g melamine and 10 g KCl were mixed and loaded in an aluminum foil-wrapped crucible. Then, four parts of the same mixture were separately calcined at 540, 570, 600, and 630°C for 2 hr with a heating rate of 10°C min<sup>-1</sup> in an air atmosphere and cooled to room temperature. Subsequently, washing the obtained products with deionized water to remove the excess alkali metal ions until the specific conductivity of the filtrate approaches zero, denoted as KCN-*x* (*x* = 540, 570, 600, 630).

**2.4. Characterization.** All samples were analyzed by X-ray diffractometer with a Cu K $\alpha$  radiation and the X-ray diffraction (XRD) patterns were recorded. The information about the structure of all samples was measured by Fourier transform infrared (FTIR) spectra using FTIR spectrometer (Thermo Fisher Nicolet iS50) in the range of 4,000–400 cm<sup>-1</sup> at a resolution of 4 cm<sup>-1</sup> with the standard disk method of KBr as reference sample. The X-ray photoelectron spectroscopy (XPS) measurements were performed with X'Pert Pro MPD spectrometer with a Cu K $\alpha$  radiation to detect elemental composition. The morphology and structure of the samples were investigated with scanning electron microscopy (SEM) (SU8010, Japan) and transmission electron microscopy (TEM) (JEOL 200CX). The porosity property of samples was obtained by nitrogen adsorption and desorption isotherms using the Micromeritics TriStar 3020 porosimeter. The Brunauer–Emmett–Teller (BET) method was used to calculate the specific surface area. The photoluminescence (PL) spectra of samples were obtained by F-4500 FL spectrometer. The photocurrent response was measured by a standard three-electrode electrochemical analyzer on the CHI 760E (CH Instruments, Inc.), and the fluorine-doped tin oxide (FTO) glass was used as coating photocatalyst, whereas the platinum wire and Ag–AgCl electrode were used as counter electrode and reference electrode. The ultraviolet–visible (UV–vis) absorption spectrum was measured by using the UV–vis spectrometer in the wavelength range of 205–800 nm.

**2.5. Photocatalytic Hydrogen Production.** The photocatalytic hydrogen production reactions were taken place in a quartz

TABLE 1: The specific data for photocatalytic H<sub>2</sub> evolution and AQE calculation.

Parameter	Description	Data
<i>S</i>	Irradiated area	38.5 cm <sup>2</sup>
<i>T</i>	Cooling temperature	20°C
<i>v</i>	Stirring speed	300 rpm
<i>t</i>	Reaction time	Determined in the test
<i>λ</i>	Wavelength	355, 420, 450, 500, and 600 nm
<i>P</i>	Wavelength (nm)	Power density (mW cm <sup>-2</sup> )
	355	5.88
	420	23.53
	450	24.52
	500	29.87
	600	31.30

reactor (300 ml). The photocatalytic reaction was performed by taking 0.1 g of catalyst powders, which were sonicated and dispersed in 90 ml deionized water, and then adding 10 ml of triethanolamine and 1 ml of chloroplatinic acid solution. Afterward, cover the quartz reactor with the lid and ensure that the reactor is completely sealed. The solution was stirred with a magnetic stirrer at a rate of 300 r min<sup>-1</sup> to disperse the substance evenly and prevent the catalyst powders from sinking at the bottom of the reaction. Moreover, the air in the reactor was removed with high purity nitrogen, first within the solution for 5 min and then above the liquid level for 10 min. After these, position the irradiation light (300 W xenon lamp) directly above the reactor and preheat it in advance. The temperature of the reaction system was maintained at 20°C by circulating cooling water to the reactor throughout the whole process. First hour of irradiation at the start of the reaction to drive the platinum loading to the surface of the catalyst powders, and then the high purity nitrogen was used to remove the hydrogen produced during the photoreduction of platinum above the liquid level about 5 min. Finally, the output hydrogen was taken each interval 1 hr and analyzed by gas chromatograph (GC 9790). Record the peak area of each hydrogen output compared to the data where the standard gas is hydrogen. The relative data for photocatalytic H<sub>2</sub> evolution and apparent quantum efficiency (AQE) calculation have been listed in Table 1.

**2.6. Quantum Efficiency of Samples.** The AQE of samples was investigated by calculating the amount of hydrogen production in a series of bandpass filters, whose  $\lambda$  = 400, 420, 450, 500, and 600 nm, under the monochromatic light exposure. Then, all the data were recorded and calculated using the following equation:

$$\begin{aligned}
 \text{AQE} &= \frac{2 \times \text{number of hydrogen molecules}}{\text{number of incident photo}} \times 100\%, \\
 &= \frac{2 \times M \times N_A}{E_{\text{total}}} \times 100\%, \\
 &= \frac{2 \times M \times N_A \times h \times c}{S \times P \times t \times \lambda} \times 100\%.
 \end{aligned} \tag{1}$$

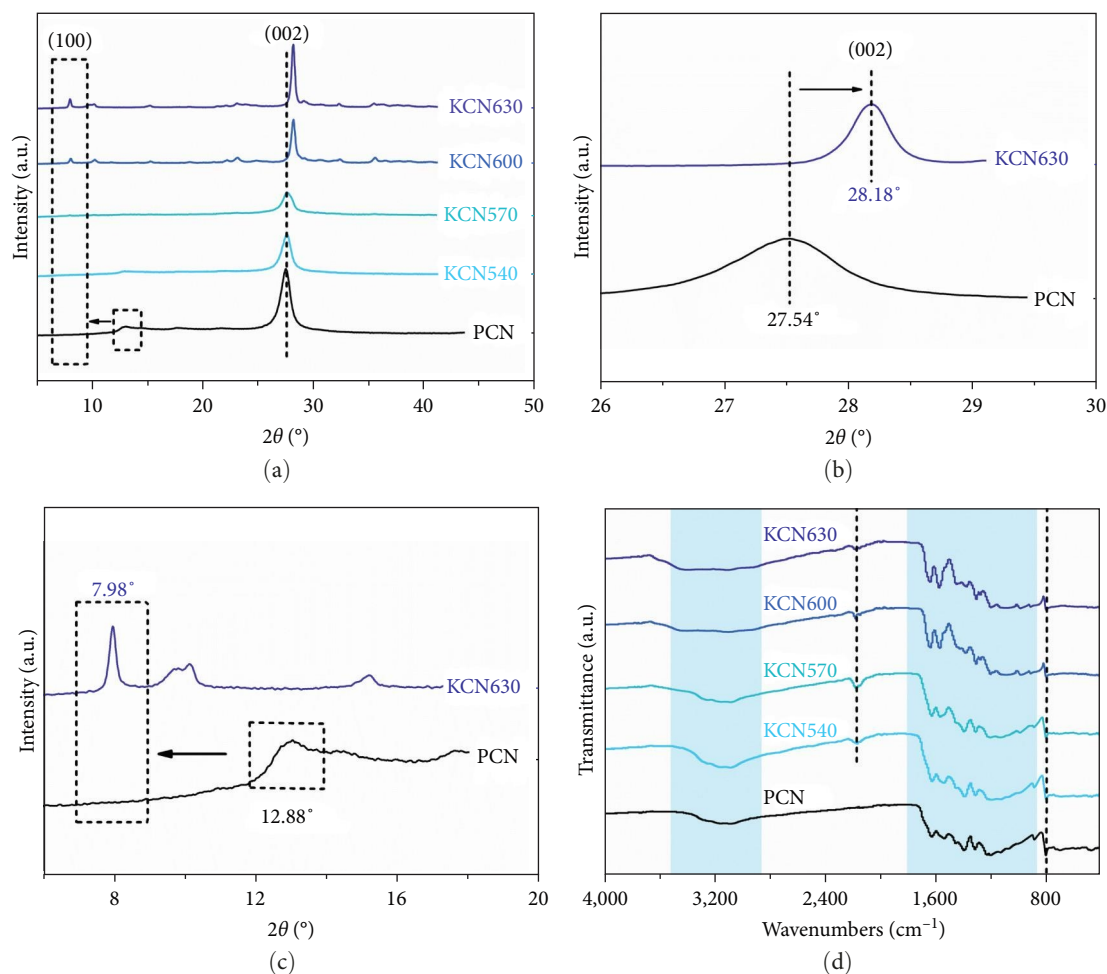


FIGURE 2: (a) XRD patterns; (b) XRD partial enlarged detail in range of  $26^\circ$ – $30^\circ$ ; (c) XRD partial enlarged detail in range of  $6^\circ$ – $20^\circ$ ; (d) FTIR spectra.

In the formula,  $M$  represents the mole number of hydrogen evolution (mol). In addition,  $N_A$ ,  $c$ , and  $h$  are the Avogadro constant ( $6.022 \times 10^{23} \text{ mol}^{-1}$ ), the speed of light ( $3.0 \times 10^8 \text{ m s}^{-1}$ ), and Planck's constant ( $6.626 \times 10^{-34} \text{ J s}$ ).  $P$  is the power density of monochromatic light irradiation and  $S$  is the irradiation area ( $\text{cm}^2$ ). The  $t$  and  $\lambda$  represent the photoreaction time (s) and wavelength of monochromatic light (m).

### 3. Results and Discussion

**3.1. Crystal and Chemical Structure Analysis.** The XRD diffraction patterns of all samples were used to identify the crystal structure, as shown in Figure 2(a). The PCN exhibits two obvious diffraction peaks located around  $13^\circ$  and  $27^\circ$ , which corresponds to (100) and (002) lattice planes. The (100) lattice plane represents in-plane structural packing motif of repeating heptazine units and (002) lattice plane corresponds to interlayer stacking of the conjugated aromatic system, respectively. The samples of KCN570, KCN600, and KCN630 show two diffraction peaks similar with PCN, indicating the analogous classical structure. However, the (002) diffraction peak upshifted from  $27.54^\circ$  of PCN to  $28.18^\circ$  of KCN630, which

reflects a higher degree of stacking order and a narrower interlayer distance (Figure 2(b)). The crystallinity of KCN570, KCN600, and KCN630 was also calculated by Jade 6.0. As a result, the proportion of crystallinity in KCN570, KCN600, and KCN630 is 18.94%, 40.98%, and 48.05%, respectively. This result indicates that the proportion of crystallinity of the samples increases with enhancing the temperature. Additionally, the (100) diffraction peak shows a downshift from  $12.88^\circ$  to  $7.98^\circ$  (Figure 2(c)), which indicates complete in-plane polymerization of heptazine units from melon-based PCN to PHI and conjugating a more crystalline structure [37]. Meanwhile, the samples' diffraction peaks at higher calcination temperatures exhibit sharper edges, resulting from better crystallinity.

The chemical structure of samples was further investigated by FTIR, as shown in Figure 2(d). No obvious difference could be observed in the spectra of samples synthesized at different calcination temperatures compared with PCN. It can be seen that all the samples show a peak at  $800 \text{ cm}^{-1}$ , corresponding to the out-of-plane bending vibration of tri-s-triazine rings. The peaks observed in the region of  $850$ – $1,800 \text{ cm}^{-1}$  correspond to the typical stretching modes of tri-s-triazine derivatives and are more intensive in K-PHI

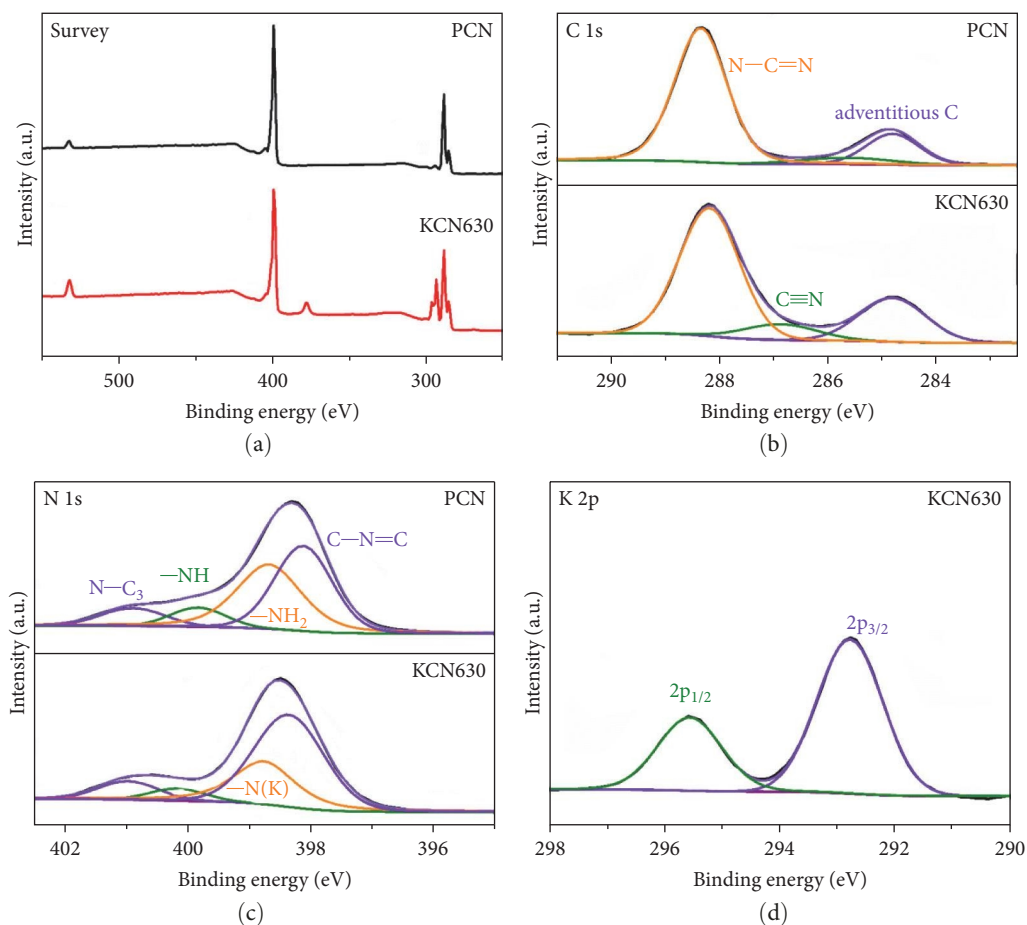


FIGURE 3: XPS spectra of PCN and KCN630: (a) survey; (b) C 1s; (c) N 1s; (d) K 2p.

samples compared with PCN. The peaks observed in the  $2,800\text{--}3,500\text{ cm}^{-1}$  can be assigned to stretching vibrations of  $\text{--NH}$  and  $\text{--OH}$ , which are resulted from the terminal amino and adsorbed  $\text{H}_2\text{O}$ . In addition, the peaks of K-PHI samples at this range are much lower than PCN, which can be attributed to the reduced content of terminal amino in the formers due to the formation of tri-*s*-triazine group crystal structure with the deeper deamination. Besides, a weak peak of crystalline CN samples at  $2,170\text{ cm}^{-1}$  can be observed, corresponding to the cyano groups [8, 38].

The valence states and chemical environments of the constituents of the samples were tested by XPS. Figure 3(a) represents the survey spectra of PCN and KCN630. The C, N, and K elements are observed in the spectra and identified as several dominant peaks, as shown in Figure 3(b)–3(d). The survey XPS spectra of all K-PHI samples show obviously similar spectra. Moreover, no peaks of other elements are organized, except for C, N, and K, meaning that all the samples kept the same chemical composition and chemical states. The C 1s spectra of PCN and KCN630 can be further deconvoluted into three peaks by Gaussian distribution, located around 288, 286.8, and 285 eV, respectively. Figure 3(b) depicts that the peak located at 288 eV is assigned to  $\text{sp}^2$ -hybridized carbon of  $\text{N-C=N}$ , which is the aromatic carbon species in tri-*s*-triazine heterocycles [37]. Two other peaks at 286.8 and 285 eV could be ascribed

to  $\text{C}\equiv\text{N}$  and carbon contaminants in the samples, respectively [39]. Figure 3(c) shows the high-resolution N 1s spectra of two samples. It could be seen that the N 1s spectra are deconvoluted into four peaks at 401, 400, 399, and 398.4 eV. The intensive peaks located at 401, 400, and 399 eV are assigned to tertiary nitrogen groups  $[\text{N-(C)}_3]$ , the terminal amino groups ( $\text{C-N-H}$ ), and the amino groups ( $\text{--NH}_2$ ). Noticeably, the binding energy of  $[\text{N-(C)}_3]$  upshift from 400.9 for PCN to 401 eV for KCN630 is owing to the interaction of N-K on account of removing terminal amino groups in construction of PHI structure. The peak at 398.4 eV is due to  $\text{sp}^2$ -hybridized atoms ( $\text{C=N-C}$ ) in the tri-*s*-triazine rings. Figure 3(d) represents the K 2p peaks of K-PHI samples, and the two dominant peaks at 295.5 and 292.7 eV are attributed to the doping of  $\text{K}^+$  in the PCN framework. In addition, it is clearly seen that the potassium alkali metal-doped PCN shows a positive shift, as shown in Figures 3(b) and 3(c), corresponding to C 1s and N 1s binding energies, which is indicated by the formation of an interaction between the doped ions and PCN aromatic ring, presumably through chemical coordination [40]. According to previous research,  $\text{K}^+$  ions doped in tri-*s*-triazine-based crystalline PCN are thought to be present between the layers of the CN unit and the ions may act to attract adjacent layers, thus leading to a reduction in layer spacing and facilitating charge transfer.

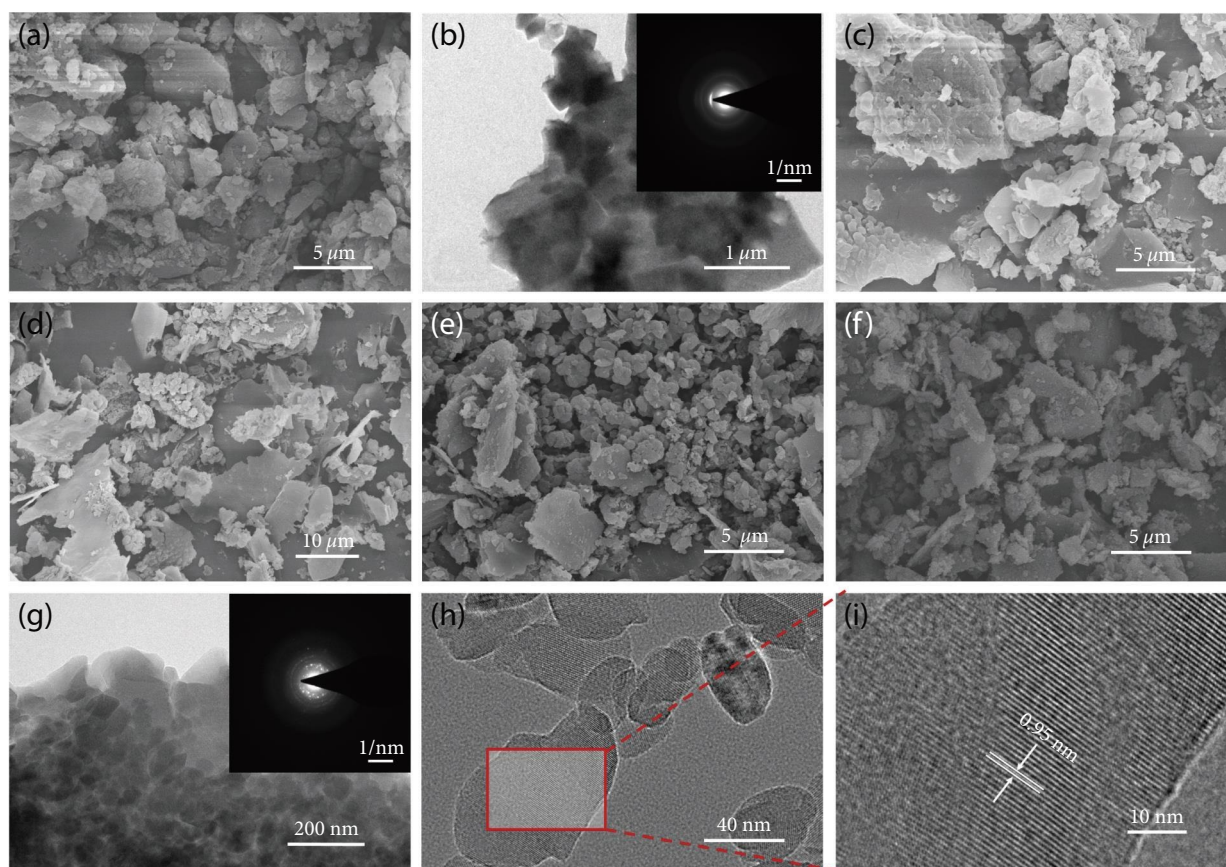


FIGURE 4: (a) SEM and (b) TEM images of PCN (insert electron diffraction patterns); SEM images of (c) KCN540, (d) KCN570, (e) KCN600, and (f) KCN630; (g) TEM images of KCN630 (insert electron diffraction patterns); (h) and (i) high-resolution TEM of KCN630.

**3.2. Morphology Characterization.** The morphology information of all samples was observed by SEM and TEM. Figures 4(a) and 4(b) show that the morphology of PCN, directly polymerized from melamine, is large, lumpy, and irregular. However, the samples, synthesized at different temperatures by mixing KCl, become more and more slack gradually with increasing calcination temperature. The cubic KCl crystals cannot be identified any more in visual (Figure 4(c)–4(f)), which result from the KCl high temperature MS penetrating between the resulting crystal particles, preventing interconnection of the particles and enhancing the dispersion of the crystals. Thus, there is little agglomeration in the product after dissolution and washing. This could effectively increase the surface area and improve the crystallinity of samples. According to the previous research, the photocatalysts with an enlarged surface area could provide more active sites and absorption sites for reaction, which are one of the most imperative reasons for enhancing the photocatalytic activity. The TEM images of KCN630 are shown in Figure 4(g)–4(i). The TEM observation also reveals the structure of samples. It can be investigated that KCN630 exhibits a two-dimensional agglomerated layer and shows a round-edged flake morphology with rolled edges. Figure 4(g) shows that each layered lamellar structure of the sample is not completely agglomerated, and irregular pores are present. This may indirectly expose more active sites in the lower

layer and increase the reaction area through pores. Furthermore, the fringe with lattice spacing of about 0.95 nm can be observed clearly in KCN630 (Figure 4(i)) on account of high crystallinity, which corresponds to the XRD diffraction peak. The difference in crystallinity between KCN630 and PCN can also be clearly observed from the electron diffraction pattern. The PCN shows the electron diffraction pattern of fuzzy diffraction ring, while that of KCN630 behaves like a speckle diffraction pattern, which indicates that the crystallinity of KCN630 is much higher than that of PCN (Figures 4(b) and 4(g), inset).

In addition, in order to prove the above conclusion, the nitrogen adsorption–desorption isotherms and pore size distribution curves of samples were measured and shown in Figures 5(a) and 5(b). The BET-specific surface areas of PCN and KCN630 are 9.12 and 26.50 m<sup>2</sup>/g, respectively. The latter is 2.9 times the former. The enlarged surface area indicates that KCN630 can offer more active sites and further confirms the higher crystallinity and dispersibility of KCN630. In comparison, the specific surface area of KCN630 is less affected by the small-size effect of the reduced particle sizes of temperature-treated K-PHI and the increased degree of coagulation, as the temperature is too high to cause significant oxidative etching effects and the smaller crystal size and more dispersed structure result in a significant increase in specific surface area. The increase in specific surface area also

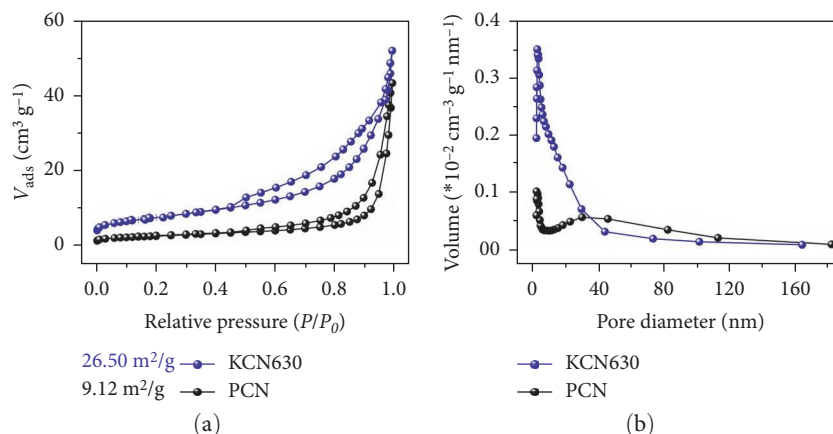


FIGURE 5: (a)  $N_2$  adsorption–desorption isotherms and (b) pore size distribution curves of samples.

means that more active sites are generated. Furthermore, a lot of mesopores with pore diameter of around 2–4 nm are measured in the KCN630 sample (Figure 5(b)), which is also beneficial to the photocatalytic  $H_2$  evolution and accords well with the SEM and TEM results.

**3.3. Optical and Photoelectrical Properties.** The optical properties play an important role in the photocatalytic activity, so the UV–vis diffuse reflectance spectra (DRS) of all samples were tested and shown in Figure 6(a). From these measurement studies, it is found that the PCN sample shows a typical n-type semiconductor with the absorption edge at 466 nm. Samples of K-PHI show integrally increased optical absorption performance when the thermal condensation temperature increases, which is attributed to the improved crystallinity and  $K^+$  doping. Therefore, the sample KCN630 exhibits the strongest light absorption activity with the absorption edge at 464 nm. This may be due to its planar lamellar structure with irregular pores, which is beneficial to the entry of light sources to enhance light absorption (see above). Furthermore, the related bandgaps are obtained by calculating the Kubelka–Munk transformed function between  $\alpha h\nu^{1/2}$  and  $h\nu$ , as shown in Figure 6(a). From the graph, the bandgaps energy of all samples can be obtained to be about 2.43, 2.48, 2.54, 2.60, and 2.59 eV, respectively. The PCN shows a large bandgap at 2.59 eV compared to samples of K-PHI, and the bandgaps of K-PHI samples are relatively narrow, resulting from the small-size effect of the reduced particle sizes of temperature-treated K-PHI and the increased degree of coagulation. In addition, the doping of  $K^+$  ions in tris-s-triazine-based crystalline PCN, as mentioned above, attracts adjacent layers and reduces the layer spacing, which is also one of the main reasons for the reduced bandgap.

The PL is a useful evidence to study the photoinduced charge separation and transfer. The PL spectra of all samples were tested, as shown in Figure 6(b). All the samples show only a kind of luminescence peak in the spectrum, and the PCN displays a strong characteristic intensity compared with K-PHI samples. In contrast, all the modified samples have similar but highly quenched PL peaks, and the peak intensity shows further weakening at increased synthesis temperature. A comparative study of the overall intensity of all samples

shows that photoinduced recombination of electrons and holes is significantly inhibited in the K-PHI crystal structure and exhibits obvious photocatalytic properties because of its lower intensity, which is ascribed to the further increased crystallinity of the former, the presence of minor defects, and the introduction of impurity levels between gaps [40]. To further understand the separation and transfer of photoinduced electron–hole, the ns-level time-resolved fluorescence decay spectra were calculated and fitted with biexponential decay kinetics, as shown in Figure 6(c) and Table 2. The average fluorescence lifetime of PCN and KCN630 is 1.04 and 1.26 ns, respectively. It is not difficult to analyze that both the lifetime components representing both short and long decay components ( $\tau_1$  and  $\tau_2$ ) of K-PHI samples are extended compared with PCN, consistent with the suppression of PL described above (Figure 6(b)). This further confirms that the recombination of light-induced electron–holes is delayed due to changes in electronic structure and increased crystallinity, thereby enhancing catalytic activity.

In addition, the photocurrent measurements could also be used to investigate the photogenerated charge separation and transfer process. The transit photocurrent responses of samples were monitored by using intermittent on-off irradiation cycles, as shown in Figure 6(d). Compared to the PCN standard, the K-PHI samples exhibit a significantly higher photocurrent intensity and strength with increasing synthesis temperature, reflecting the better separation and transfer of photoinduced electron holes, in line with the above analysis. The sample of KCN630 shows the highest photocurrent, which is beneficial to photocatalytic activity. The electron paramagnetic resonance (EPR) spectra results of the samples are shown in Figure 6(e). After light irradiation for 5 min, KCN630 exhibits a stronger EPR signal than PCN, indicating that more photoelectrons were generated in KCN630, which is beneficial for the photocatalytic  $H_2$  production reaction. In addition, KCN630 also shows a larger surface photovoltage intensity upon PL (Figure 6(f)), which is also attributed to the higher crystallinity of the former. This result is an agreement with the EPR.

**3.4. Photocatalytic Activity.** The photocatalytic hydrogen evolution activity of all samples was tested under visible light irradiation ( $\lambda \geq 420$  nm). All samples demonstrate a stable

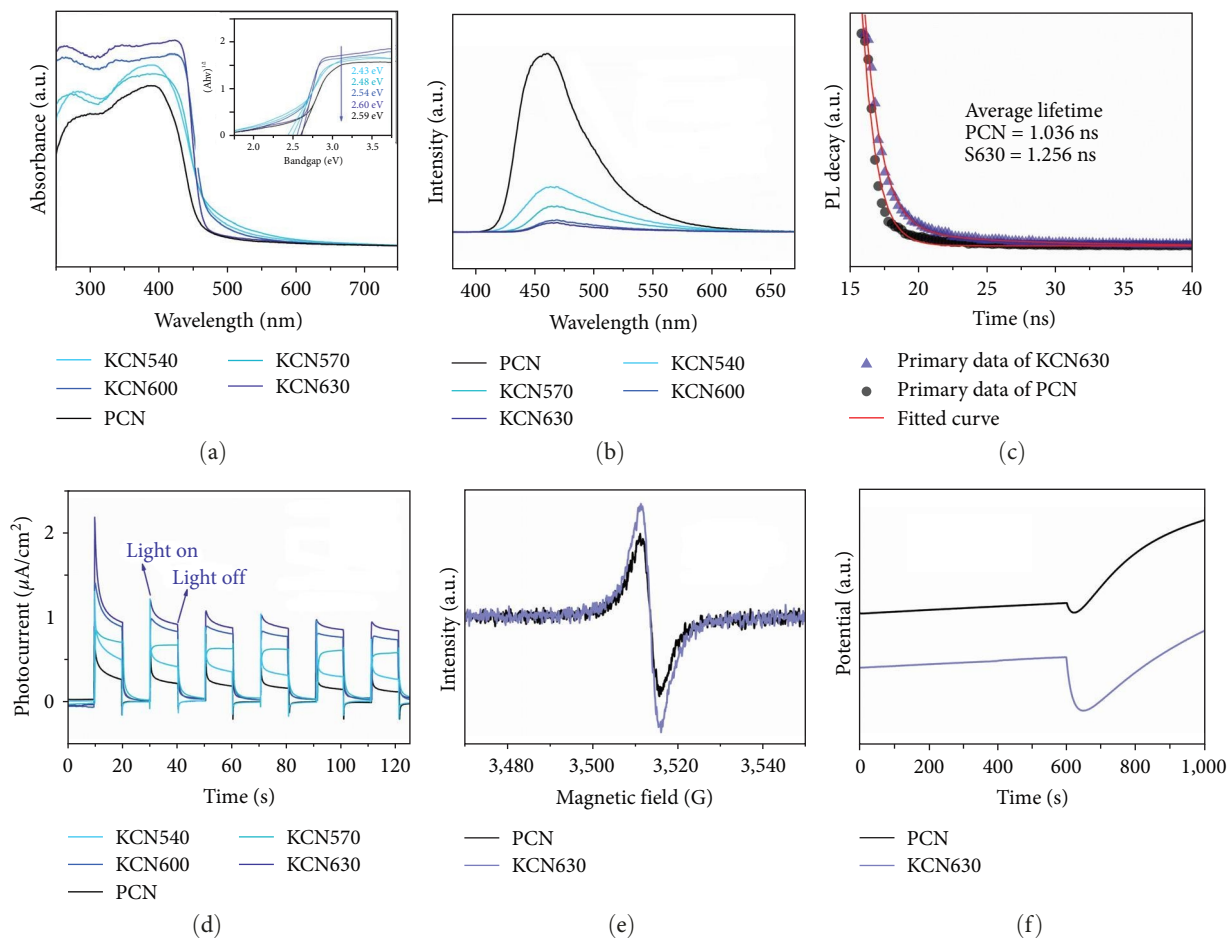


FIGURE 6: (a) UV-vis DRS spectra and insert figure of Kubelka–Munk transformed function, (b) PL spectra, (c) ns-level time-resolved fluorescence lifetime spectra, (d) photocurrent of samples, (e) EPR spectra, and (f) surface photovoltage.

TABLE 2: The exponential fitting results of ns-level time-resolved fluorescence spectra.

Sample	$\tau_1$ (ns)	A1 (%)	$\tau_2$ (ns)	A2 (%)	$\tau_A$ (ns)
PCN	1.04	50.00	1.04	50.00	1.04
KCN630	8.58	0.01	1.26	99.99	1.26

and linear hydrogen evolution reaction for 4 hr (Figure 7(a)). The average hydrogen production per hour of the samples is shown in Figure 7(b). As shown in Figure 7(b), it is clearly shown that the hydrogen production rate of PCN is about  $0.057 \text{ mmol h}^{-1} \text{ g}^{-1}$  and the K-PHI at 540, 570, 600, and  $630^\circ\text{C}$  is about 0.073, 0.141, 0.522, and  $1.798 \text{ mmol h}^{-1} \text{ g}^{-1}$ , respectively. Obviously, the results show that the K-PHI prepared at  $630^\circ\text{C}$  exhibits the highest photocatalytic activity, which is 31.5, 24.6, 12.8, and 3.4 times that of PCN, KCN540, KCN570, and KCN600, respectively, corresponding to the improved photoinduced charge separation and transfer due to high crystallinity. There is a clear correlation between the photocatalytic activity and the synthesis temperature of the samples, as shown by the fact that the higher the temperature of the synthesized sample, the stronger the photocatalytic activity of the sample, which is consistent with the specific surface area. Thus, it can be proved that the synthesis

temperature of the sample affects the photocatalytic activity. The higher calcination temperature may enhance the higher photocatalytic hydrogen production efficiency, benefiting from the high crystallinity and nanostructured morphology.

In order to determine the stability of the KCN630 sample, the photocatalytic experiments with a period of 4 hr were carried out over 12 hr, and the results are shown in Figure 7(c). It is worth noting that the three-cycle test for K-PHI shows clear similarities, demonstrating their good stability in photocatalytic hydrogen evolution. Furthermore, the AQE value of KCN630 was also measured at different monochromatic light irradiations (different wavelength ranges) and shown in Figure 7(d), which is consistent with its UV-vis absorption spectrum, demonstrating that the photocatalytic  $\text{H}_2$  evolution of K-PHI depends on the wavelength of the light.

To assess its performance objectively, we compare it with the heptazine-based CN photocatalysts reported so far. As shown in Figure 8, although the photocatalytic activity of KCN630 is less than the nanoscale crystalline CN samples, they are still better than most heptazine-based crystalline CN materials with plain morphology [8, 26, 29, 31, 41–49].

The photocatalytic  $\text{H}_2$  evolution mechanism is illustrated in Figure 9. The mechanism of photocatalytic  $\text{H}_2$  evolution can

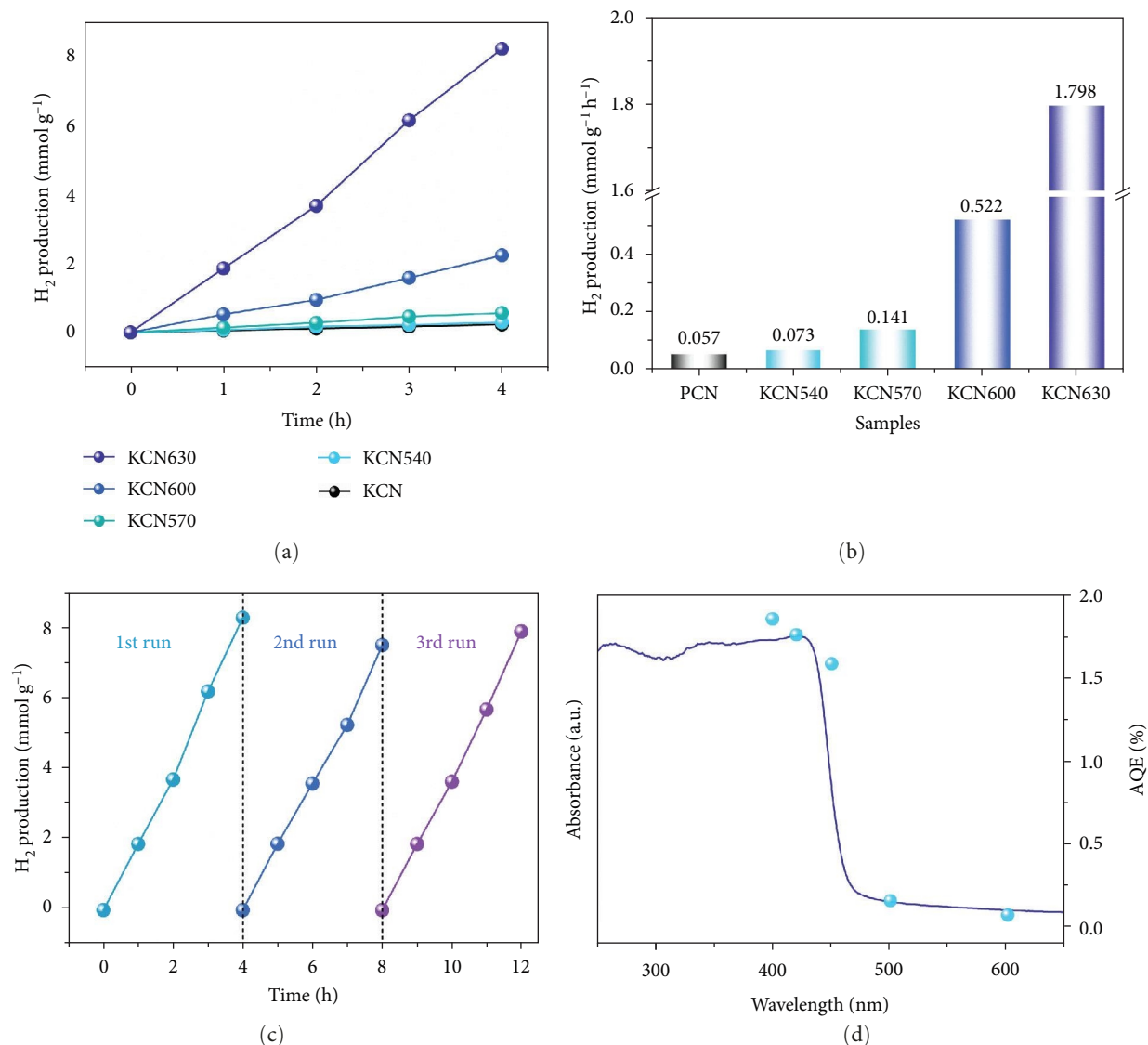


FIGURE 7: (a) Time-varying photocatalytic  $H_2$  production and (b) average hydrogen production rate of all samples; (c) cycling hydrogen production test; (d) wavelength-dependent AQE (right axis) and UV-vis light absorption spectrum (left axis) of KCN630.

mainly be stated in three steps: photoinduced electron holes were generated from samples under visible light irradiation; the separation and transfer of photoinduced electron holes; and surface redox reaction. In general, the inherent nature of regulation to improve the photocatalytic  $H_2$  evolution activity was focused on these three processes. In this study, the formation of crystalline structure and the improved photocatalytic  $H_2$  evolution activity are mainly attributed to the more effective deamination. The electrons and holes are generated under visible light irradiation, and the photoinduced holes are quenched by a sacrificial electron donor (triethanolamine) in solution. Then, the photoinduced electrons quickly transfer to Pt nanoparticle co-catalyst to reduce  $H^+$  into  $H_2$ . The samples exhibit gradually improved photocatalytic  $H_2$  evolution rate with the enhancement of temperature, which is due to that higher temperature can promote the polymerization of in-plane heptazine units and further promote the separation and transfer of photoinduced charges.

#### 4. Conclusions

In summary, the effect of temperature on the crystallinity of heptazine-based crystalline CN was studied by one-step synthesis at different temperatures. All heptazine-based crystalline CN (K-PHI samples) illustrates highly boosted photocatalytic activity compared with PCN. The improvement of photocatalytic activity is mainly attributed to the enhanced charge separation and active sites owing to both high crystallinity and nanostructured morphology. Additionally, the photocatalytic  $H_2$  evolution rate of K-PHI is gradually enhanced with the improvement of calcination temperature, which is attributed to the gradually improved crystallinity. The optimal sample (synthesized at 630°C) exhibits the highest photocatalytic  $H_2$  evolution rate of 1.798 mmol  $h^{-1} g^{-1}$ , which is 31.5 times that of bulk PCN. This work confirms that increasing the temperature within a certain range can make progress in the microstructure of crystalline CN, i.e.,

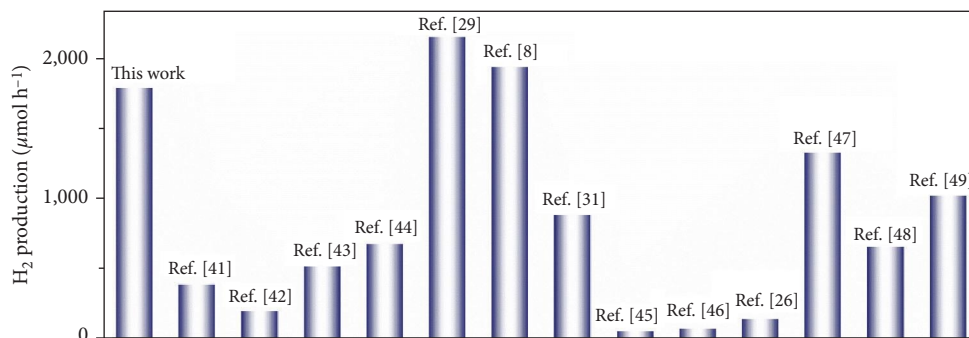


FIGURE 8: Comparison of active wavelength with the KCN630 and reported heptazine-based crystalline carbon nitride photocatalysts.

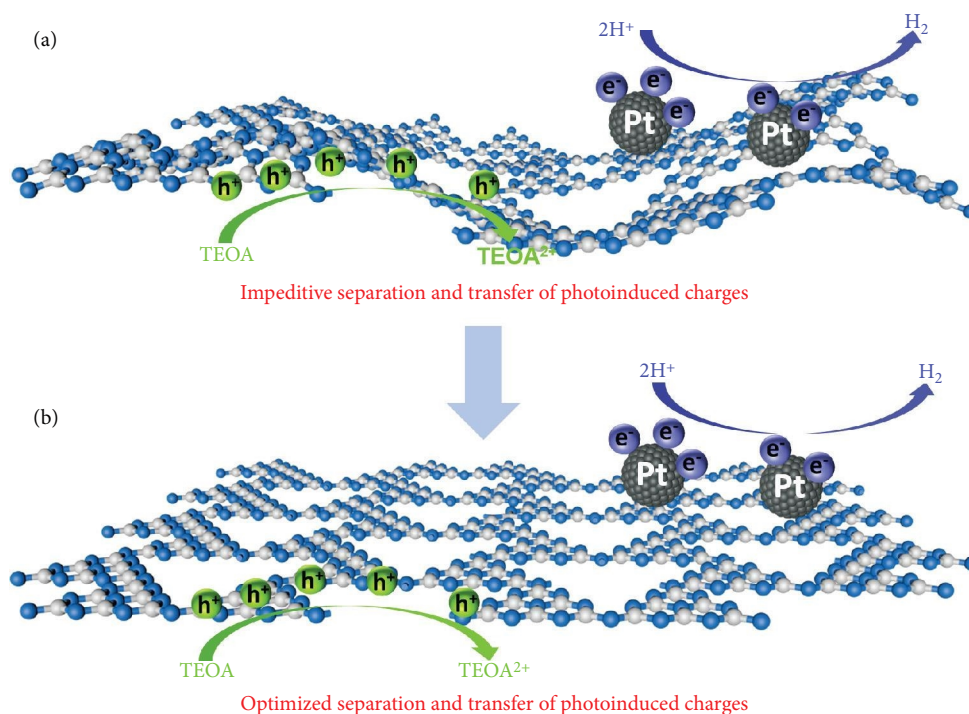


FIGURE 9: Schematic illustration of the photocatalytic H<sub>2</sub> evolution on (a) PCN and (b) K-PHI.

crystallinity, which can enhance the photocatalytic activity and this mechanism may promote the crystallinity regulation of heptazine-based crystalline CN.

### Data Availability

Data available on request from the authors.

### Conflicts of Interest

The authors declare that they have no conflicts of interest.

### Acknowledgments

The authors gratefully acknowledge the support from the National Key R&D Program of China (2021YFA0715900), the Hubei Three Gorges Laboratory Open/Innovation Fund (SC211010), the Natural Science Foundation of

Zhejiang Province (LQY18D020001), the National Natural Science Foundation of China (41502030), and the Science and Technology Department of Hubei Province of China (2017ACA091).

### References

- [1] J. Zhu, P. Xiao, H. Li, and S. A. C. Carabineiro, "Graphitic carbon nitride: synthesis, properties, and applications in catalysis," *ACS Applied Materials & Interfaces*, vol. 6, no. 19, pp. 16449–16465, 2014.
- [2] Z. Mo, X. She, Y. Li et al., "Synthesis of g-C<sub>3</sub>N<sub>4</sub> at different temperatures for superior visible/UV photocatalytic performance and photoelectrochemical sensing of MB solution," *RSC Advances*, vol. 5, no. 123, pp. 101552–101562, 2015.
- [3] L. Ge, C. Han, X. Xiao, and L. Guo, "In situ synthesis of cobalt-phosphate (Co-Pi) modified g-C<sub>3</sub>N<sub>4</sub> photocatalysts with enhanced photocatalytic activities," *Applied Catalysis B: Environmental*, vol. 142–143, pp. 414–422, 2013.

- [4] S. Martha, A. Nashim, and K. M. Parida, "Facile synthesis of highly active g-C<sub>3</sub>N<sub>4</sub> for efficient hydrogen production under visible light," *Journal of Materials Chemistry A*, vol. 1, no. 26, pp. 7816–7824, 2013.
- [5] Y. Wang, X. Wang, and M. Antonietti, "Polymeric graphitic carbon nitride as a heterogeneous orgaeocatalysti from photochemistry to multipurpose catalysis to sustainable chemistry," *Angewandte Chemie International Edition*, vol. 51, no. 1, pp. 68–89, 2012.
- [6] X. Wang, K. Maeda, A. Thomas et al., "A metal-free polymeric photocatalyst for hydrogen production from water under visible light," *Nature Materials*, vol. 8, pp. 76–80, 2009.
- [7] Y.-P. Yuan, S.-W. Cao, Y.-S. Liao, L.-S. Yin, and C. Xue, "Red phosphor/g-C<sub>3</sub>N<sub>4</sub> heterojunction with enhanced photocatalytic activities for solar fuels production," *Applied Catalysis B: Environmental*, vol. 140–141, pp. 164–168, 2013.
- [8] W. Wang, Z. Shu, J. Zhou, D. Meng, Z. Zhao, and T. Li, "Facile synthesis and microstructure modulation of crystalline polymeric carbon nitride for highly boosted photocatalytic hydrogen evolution," *Journal of Materials Chemistry A*, vol. 8, no. 14, pp. 6785–6794, 2020.
- [9] Z. Zhao, X. Wang, Z. Shu et al., "Facile preparation of hollow-nanosphere based mesoporous g-C<sub>3</sub>N<sub>4</sub> for highly enhanced visible-light-driven photocatalytic hydrogen evolution," *Applied Surface Science*, vol. 455, pp. 591–598, 2018.
- [10] X. Wang, Z. Zhao, Z. Shu et al., "One-pot synthesis of meta-kaolin/g-C<sub>3</sub>N<sub>4</sub> composite for improved visible-light photocatalytic H<sub>2</sub> evolution," *Applied Clay Science*, vol. 166, pp. 80–87, 2018.
- [11] W. Wang, Z. Shu, J. Zhou et al., "Halloysite-derived mesoporous g-C<sub>3</sub>N<sub>4</sub> nanotubes for improved visible-light photocatalytic hydrogen evolution," *Applied Clay Science*, vol. 158, pp. 143–149, 2018.
- [12] Y. Tan, Z. Shu, J. Zhou, T. Li, W. Wang, and Z. Zhao, "One-step synthesis of nanostructured g-C<sub>3</sub>N<sub>4</sub>/TiO<sub>2</sub> composite for highly enhanced visible-light photocatalytic H<sub>2</sub> evolution," *Applied Catalysis B: Environmental*, vol. 230, pp. 260–268, 2018.
- [13] Z. Tong, D. Yang, T. Xiao, Y. Tian, and Z. Jiang, "Biomimetic fabrication of g-C<sub>3</sub>N<sub>4</sub>/TiO<sub>2</sub> nanosheets with enhanced photocatalytic activity toward organic pollutant degradation," *Chemical Engineering Journal*, vol. 260, pp. 117–125, 2015.
- [14] X. Wen, W. Wang, Q. Ye et al., "One-step synthesis of rice husk carbon with dangling CC bonds loaded g-C<sub>3</sub>N<sub>4</sub> for enhanced photocatalytic degradation," *Journal of Cleaner Production*, vol. 272, Article ID 122625, 2020.
- [15] Z. Sun, H. Wang, Z. Wu, and L. Wang, "g-C<sub>3</sub>N<sub>4</sub> based composite photocatalysts for photocatalytic CO<sub>2</sub> reduction," *Catalysis Today*, vol. 300, pp. 160–172, 2018.
- [16] S. Ye, R. Wang, M.-Z. Wu, and Y.-P. Yuan, "A review on g-C<sub>3</sub>N<sub>4</sub> for photocatalytic water splitting and CO<sub>2</sub> reduction," *Applied Surface Science*, vol. 358, Part A, pp. 15–27, 2015.
- [17] F. Wang, Y. Feng, P. Chen et al., "Photocatalytic degradation of fluoroquinolone antibiotics using ordered mesoporous g-C<sub>3</sub>N<sub>4</sub> under simulated sunlight irradiation: kinetics, mechanism, and antibacterial activity elimination," *Applied Catalysis B: Environmental*, vol. 227, pp. 114–122, 2018.
- [18] M. Ghanbari and M. Salavati-Niasari, "Copper iodide decorated graphitic carbon nitride sheets with enhanced visible-light response for photocatalytic organic pollutant removal and antibacterial activities," *Ecotoxicology and Environmental Safety*, vol. 208, Article ID 111712, 2021.
- [19] X. Zhang, H. Wang, H. Wang et al., "Single-layered graphitic-C<sub>3</sub>N<sub>4</sub> quantum dots for two-photon fluorescence imaging of cellular nucleus," *Advanced Materials*, vol. 26, no. 26, pp. 4438–4443, 2014.
- [20] F. Fina, S. K. Callear, G. M. Carins, and J. T. S. Irvine, "Structural investigation of graphitic carbon nitride via XRD and neutron diffraction," *Chemistry of Materials*, vol. 27, no. 7, pp. 2612–2618, 2015.
- [21] X. Wang, S. Blechert, and M. Antonietti, "Polymeric graphitic carbon nitride for heterogeneous photocatalysis," *ACS Catalysis*, vol. 2, no. 8, pp. 1596–1606, 2012.
- [22] A. Yuan, H. Lei, F. Xi et al., "Graphene quantum dots decorated graphitic carbon nitride nanorods for photocatalytic removal of antibiotics," *Journal of Colloid and Interface Science*, vol. 548, pp. 56–65, 2019.
- [23] H. Schlomberg, J. Kröger, G. Savasci et al., "Structural insights into poly(heptazine imides): a light-storing carbon nitride material for dark photocatalysis," *Chemistry of Materials*, vol. 31, no. 18, pp. 7478–7486, 2019.
- [24] M. B. Mesch, K. Bärwinkel, Y. Krysiak et al., "Solving the hydrogen and lithium substructure of poly(triazine imide)/LiCl using NMR crystallography," *Chemistry—A European Journal*, vol. 22, no. 47, pp. 16878–16890, 2016.
- [25] H. H. Ou, L. Lin, Y. Zheng, P. Yang, Y. Pang, and X. Wang, "Tri-s-triazine-based crystalline carbon nitride nanosheets for an improved hydrogen evolution," *Advanced Materials*, vol. 29, no. 22, Article ID 1700008, 2017.
- [26] Z. Zeng, H. Yu, X. Quan, S. Chen, and S. Zhang, "Structuring phase junction between tri-s-triazine and triazine crystalline C<sub>3</sub>N<sub>4</sub> for efficient photocatalytic hydrogen evolution," *Applied Catalysis B: Environmental*, vol. 227, pp. 153–160, 2018.
- [27] Y. Li, D. Zhang, J. Fan, and Q. Xiang, "Highly crystalline carbon nitride hollow spheres with enhanced photocatalytic performance," *Chinese Journal of Catalysis*, vol. 42, no. 4, pp. 627–636, 2021.
- [28] J. Liu, W. Fu, Y. Liao, J. Fan, and Q. Xiang, "Recent advances in crystalline carbon nitride for photocatalysis," *Journal of Materials Science and Technology*, vol. 91, pp. 224–240, 2021.
- [29] W. Wang, Z. Shu, Z. Liao et al., "Sustainable one-step synthesis of nanostructured potassium poly(heptazine imide) for highly boosted photocatalytic hydrogen evolution," *Chemical Engineering Journal*, vol. 424, Article ID 130332, 2021.
- [30] X. Zhang, C. Yu, J. Guan et al., "Polymeric heptazine imide by O doping and constructing van der Waals heterostructures for photocatalytic water splitting: a theoretical perspective from transition dipole moment analyses," *Physical Chemistry Chemical Physics*, vol. 22, no. 18, pp. 9915–9922, 2020.
- [31] Y. Li, F. Gong, Q. Zhou, X. Feng, J. Fen, and Q. Xiang, "Crystalline isotype heptazine-/triazine-based carbon nitride heterojunctions for an improved hydrogen evolution," *Applied Catalysis B: Environmental*, vol. 268, Article ID 118381, 2020.
- [32] X. Fan, Y. Yao, Y. Xu, L. Yu, and C. Qiu, "Visible-light-driven photocatalytic hydrogenation of olefins using water as the H source," *ChemCatChem*, vol. 11, no. 11, pp. 2596–2599, 2019.
- [33] F. He, M. Wang, L. Luo, Z. Wang, S. Peng, and Y. Li, "Directional modulation of triazine and heptazine based carbon nitride for efficient photocatalytic H<sub>2</sub> evolution," *Applied Surface Science*, vol. 562, Article ID 150103, 2021.
- [34] H. Kato, K. Asakura, and A. Kudo, "Highly efficient water splitting into H<sub>2</sub> and O<sub>2</sub> over lanthanum-doped NaTaO<sub>3</sub> photocatalysts with high crystallinity and surface nanostructure," *Journal of the American Chemical Society*, vol. 125, no. 10, pp. 3082–3089, 2003.

- [35] S. M. Menke and R. J. Holmes, "Exciton diffusion in organic photovoltaic cells," *Energy & Environmental Science*, vol. 7, no. 2, pp. 499–512, 2014.
- [36] Y. Chen, B. Wang, S. Lin, Y. Zhang, and X. Wang, "Activation of  $n \rightarrow \pi^*$  transitions in two-dimensional conjugated polymers for visible light photocatalysis," *The Journal of Physical Chemistry C*, vol. 118, no. 51, pp. 29981–29989, 2014.
- [37] L. Lin, H. Ou, Y. Zhang, and X. Wang, "Tri-*s*-triazine-based crystalline graphitic carbon nitrides for highly efficient hydrogen evolution photocatalysis," *ACS Catalysis*, vol. 6, no. 6, pp. 3921–3931, 2016.
- [38] H. Wang, Y. Bian, J. Hu, and L. Dai, "Highly crystalline sulfur-doped carbon nitride as photocatalyst for efficient visible-light hydrogen generation," *Applied Catalysis B: Environmental*, vol. 238, pp. 592–598, 2018.
- [39] Y. Wang, Y. Li, W. Ju et al., "Molten salt synthesis of water-dispersible polymeric carbon nitride nanoseaweeds and their application as luminescent probes," *Carbon*, vol. 102, pp. 477–486, 2016.
- [40] J. Jiang, S. Cao, C. Hu, and C. Chen, "A comparison study of alkali metal-doped  $g\text{-C}_3\text{N}_4$  for visible-light photocatalytic hydrogen evolution," *Chinese Journal of Catalysis*, vol. 38, no. 12, pp. 1981–1989, 2017.
- [41] G. Zhang, Y. Xu, C. He, P. Zhang, and H. Mi, "Oxygen-doped crystalline carbon nitride with greatly extended visible-light-responsive range for photocatalytic  $\text{H}_2$  generation," *Applied Catalysis B: Environmental*, vol. 283, Article ID 119636, 2021.
- [42] X. Zhou, Y. Shi, W. Xu et al., "Ultra-thin deaminated tri-*s*-triazine-based crystalline nanosheets with high photocatalytic hydrogen evolution performance," *Journal of Alloys and Compounds*, vol. 827, Article ID 154307, 2020.
- [43] V. V. Shvalagin, G. V. Korzhak, S. Y. Kuchmiy, M. A. Skoryk, O. V. Selyshchev, and D. R. T. Zahn, "Facile preparation and high photocatalytic activity of crystalline graphitic carbon nitride in hydrogen evolution from electron donor solutions under visible light," *Journal of Photochemistry and Photobiology A: Chemistry*, vol. 390, Article ID 112295, 2020.
- [44] Y. Li, D. Zhang, X. Feng, and Q. Xiang, "Enhanced photocatalytic hydrogen production activity of highly crystalline carbon nitride synthesized by hydrochloric acid treatment," *Chinese Journal of Catalysis*, vol. 41, no. 1, pp. 21–30, 2020.
- [45] Y. Xua, C. Qiu, X. Fan et al., " $\text{K}^+$ -induced crystallization of polymeric carbon nitride to boost its photocatalytic activity for  $\text{H}_2$  evolution and hydrogenation of alkenes," *Applied Catalysis B: Environmental*, vol. 268, Article ID 118457, 2020.
- [46] Y. Wang, X. Zhou, W. Xu et al., "Zn-doped tri-*s*-triazine crystalline carbon nitrides for efficient hydrogen evolution photocatalysis," *Applied Catalysis A: General*, vol. 582, Article ID 117118, 2019.
- [47] Y. Wang, S. Zhao, Y. Zhang et al., "One-pot synthesis of K-doped  $g\text{-C}_3\text{N}_4$  nanosheets with enhanced photocatalytic hydrogen production under visible-light irradiation," *Applied Surface Science*, vol. 440, pp. 258–265, 2018.
- [48] J. Yang, Y. Liang, K. Li et al., "One-step synthesis of novel  $\text{K}^+$  and cyano groups decorated triazine-/heptazine-based  $g\text{-C}_3\text{N}_4$  tubular homojunctions for boosting photocatalytic  $\text{H}_2$  evolution," *Applied Catalysis B: Environmental*, vol. 262, Article ID 118252, 2019.
- [49] L. Wang, Y. Hong, E. Liu et al., "Rapid polymerization synthesizing high-crystalline  $g\text{-C}_3\text{N}_4$  towards boosting solar photocatalytic  $\text{H}_2$  generation," *International Journal of Hydrogen Energy*, vol. 45, no. 11, pp. 6425–6436, 2020.